Facultade de Física
Grao en Física

Traballo de Fin de Grao

Analysis of charged particle multiplicity associated with ϕ mesons in proton-nucleus collisions at the LHCb experiment

---

Autor:
Alberto Saborido Patiño

Titor:
Cibrán Santamarina Ríos
Física Átomica, Molecular e Nuclear, Departamento de Física de Partículas

Cotitor:
Oscar Boente García
Física Átomica, Molecular e Nuclear, Departamento de Física de Partículas

Febreiro 2022

Agradecementos

Especial agradecemento ós meus titores Cibrán Santamarina Ríos e Oscar Boente García. Por guiarme neste proxecto e pola súa constante dispoñibilidade e cercanía. Á prof.ª. Elena González Ferreiro, por aportar a sua axuda na interpretación fenomenolóxica dos resultados. Por último, agradecer á miña familia e ós meus compañeiros de grao por todo o apoio ofrecido nestes anos.

Abstract

Proton-lead collisions at $\sqrt{s_{NN}} = 5.02$ TeV were analysed in order to study the dependency between the production of ϕ mesons and the number of charged particles produced in the process, called multiplicity. The study of the multiplicity dependence on the production of particles with strangeness is important for the understanding of the formation and evolution of the Quark Gluon Plasma. For this purpose, the observables are constructed in such a way that the detector efficiency does not bias the study. A ratio between different multiplicity ranges (RCP, Ratio Central-Peripheral) and a double ratio between the RCPs corresponding to the different colliding beams configurations are calculated. The obtained results are compared with other observations and discussed as a consequence of some physical mechanism, such as the Cronin effect or saturation effects.

Keywords: LHC*b*, HEP, heavy-ion physics, ϕ-meson, strangeness, multiplicity, charged particles

Resumo

Analizáronse colisións protón plomo a $\sqrt{s_{NN}} = 5,02$ TeV para estudar a relación entre a produción de mesóns ϕ e o número de partículas cargadas producidas no proceso, denominado multiplicidade. O estudo da depencencia da multiplicidade na produción de partículas con extrañeza é importante para o entendemento da formación e evolución do Plasma de Quarks-Gluóns. Para facelo, os observables son contruídos de forma que a eficiencia do detector non supoña un nesgo nas observacións. Calcúlase o cociente entre medidas a diferente muliplicidade (RCP, *Ratio Central-Peripheral*) e un dobre cociente entre os RCPs correspondentes ás diferetnes configuracións dos feixes que colisionan. Os resultados obtidos son comparados con outras observacións e discutidos como consecuencia dalgúns mecanismos físicos, como o efecto Cronin ou efectos de saturación.

Resumen

Se han analizado colisiones protón plomo a $\sqrt{s_{NN}} = 5,02$ TeV para estudiar la relación entre la producción de mesones ϕ y el número de partículas cargadas producidas en el proceso, denominado multiplicidad. El estudio de la dependencia de la multiplicidad en la producción de partículas con extrañeza es importante para el entendimiento de la formación y evolución del Plasma de Quarks-Gluones. Para ello, los observables son construidos de forma que la eficiencia del detector no suponga un sesgo en el estudio. Se calcula un cociente entre medidas a diferente multiplicidad (RCP, *Ratio Central-Peripheral*) y un doble cociente entre los RCPs correspondientes a las diferentes configuraciones de los haces que colisionan. Los resultados obtenidos son comparados con otras observaciones y discutidos como consecuencia de algunos mecanismos físicos, como el efecto Cronin o efectos de saturación.

Contents

1 Introduction

In this dissertation, an analysis of the ϕ meson production as function of the multiplicity of charged particles in proton-lead collisions is performed. The study is carried out with the LHC*b* detector at CERN. The detector features and the detection method are described in section 2. After presenting the data analysis in section 3, the results and conclusions can be found in section 4 and 5, respectively.

First, a theoretical introduction is presented. Some theoretical context, as well as the definition of some important concepts that are essential in the analysis are discussed below.

1.1 Theoretical picture

Hadronic matter is formed by quarks interacting among them through the strong force. The mediators of the strong force are gluons. The theoretical framework which describes the strong force is *Quantum Chromodynamics* (QCD). Under this framework, hadrons are asymptotic states at small temperatures and densities.

QCD describes quark and gluon interactions as a function of colour charge. Quarks and gluons have colour charge (that can be red, green or blue), but all free hadrons are colourless objects. This constitutes a fundamental property of quark interactions, which is denominated colour confinement. This property restricts free particles to be colourless, so it forbids the existence of free quarks or gluons.

Due to its nature, the strong force between quarks decreases (increases) as the distance between them becomes smaller (bigger). Thus, at very high pressure and temperature, the strong attraction disappears and a deconfined state is reached. This state of matter, which has been proven to have a fluid behaviour, is called Quark-Gluon Plasma (QGP) and can be recreated in high energy collisions.

The Standard Model of Cosmology predicts that until a few milliseconds after the Big Bang, the universe was in a QGP state. Thus, the study of this state of matter is a very important step in our understanding of the properties and evolution of the Universe [1].

There are different quarks classified by flavour: up (u), down (d), charm (c), strange (s), top (t) and beauty (b). Some studies sustain that the production of particles with strangeness is a good indicator of QGP presence [2]. This is because creating hadrons composed of strange (anti-)quarks require some initial energy, while in the QGP they are readily available. For this reason, strange antibaryons and ϕ-mesons are probes of QGP presence at hadronisation.

1.2 Motivation

On high energy heavy-ion ($A-A$) collisions, the deconfined QGP state of matter is thought to be recreated, reaching kinetic and even flavor chemical equilibrium [3]. This statement has been experimentally observed through many observations, such as the strangeness enhancement that the QGP presence should produce [4]. Experimentally, such QGP state

can be characterised with the produced particle yields. The measurement of hadronic resonance yields provides an approach to study the particle production mechanisms and the characterisation of the dynamic evolution of the QGP. Therefore, such analyses conform a way of experimentally studying the phase transition predicted by QCD from ordinary matter to a deconfined QGP.

In heavy-ion collisions, there is a strong relation between the so called centrality of the collision and the QGP evolution and subsequent hadronisation . The centrality in $A-A$ collisions can be understood as the geometric overlap of the two colliding nuclei [5], while there is no fundamental definition of centrality for proton-nucleus ($p-A$) collisions. Nevertheless, centrality is highly correlated with the number of charged particles produced in the collision. Thus, the proton-nucleus collisions can also be classified by their centrality due to the number of produced charged particles.

The centrality of heavy-ion collisions and the QGP presence is believed to affects to the angular correlations of the produced particles and its flow. Recently, particle correlations have been measured for $p-p$ and $p-A$ collisions, obtaining similar structures to those that were believed to be caused by the presence of QGP measured in $A-A$ collisions [6]. The precise origin of this effects is not fully understood, but assuming that no QGP is formed on $p-A$ collisions, an alternative explanation is needed.

A good approach to study this type of phenomena is to measure the production of certain resonances with strangeness and study its dependence on the multiplicity of the process, this is to say, the total number of charged particles measured in the interaction. As it is already mentioned, that quantity is highly correlated with the centrality of the collision in $A-A$ collisions. Recent studies have revealed that in high multiplicity $p-$Pb collisions the yield of strange particles increases, approaching the conditions in Pb-Pb collisions (where the QGP is in principle formed) [7].

Having established the context, this analysis has two main goals:

- Report an experimental measurement of strangeness production on proton-lead collisions by measuring the ϕ meson yields in different multiplicity classes. The measurement can then be used to compare with theoretical models or results from future experiments.
- Verify if the results can be understood as a consequence of the possible appearance of some phenomena like the reach of the **saturation region** and the **Cronin effect**, concepts that will be presented in the following section. If the measured effects can be explained through these phenomena it would mean that, as it is expected by the theoretical models, such effects are not originated by the collective expansion associated to the QGP fluid system, as it happens on heavy-ion collisions. This measurement would also help to interpret heavy-ion collisions measurements, where QGP presence is expected, helping to discern between effects coming from the evolution of the QGP and other ones like the above mentioned.

1.3 Kinematics of the collisions

The proton-lead (p−Pb) collisions studied in this analysis are produced by two beams of protons and lead nuclei moving in opposite directions that collide in the LHCb detector. As it is further explained in section 2, the detector covers a small solid angle in the direction of one of the beams. Since both the colliding beams and the solid angle coverage of the detector are asymmetric, two configurations of the collisions are possible: pPb (so called forward) if the proton beam moves in the detector acceptance direction or Pbp (so called backward) if the lead nucleus beam does. In Figure 1 the two different configurations of the colliding beams are represented.

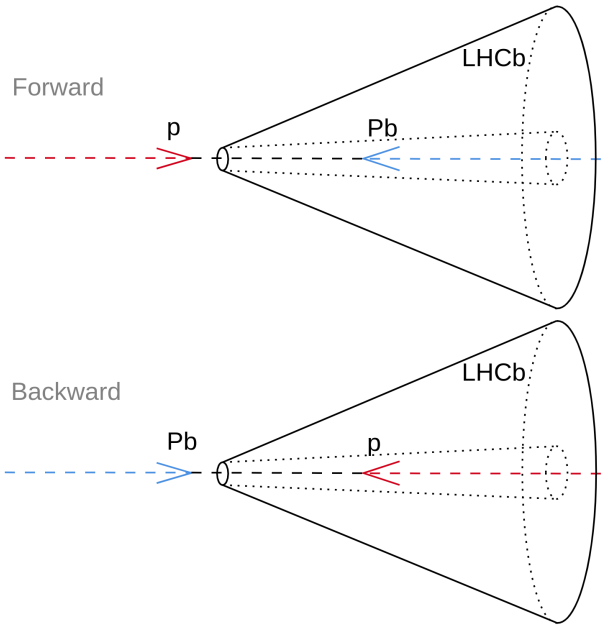

Figure 1: Representation of the two possible beam configurations: forward (pPb) at top and backward (Pbp) at bottom.

In high energy collisions the centre of mass energy required to produce a certain particle has to be greater than the sum of the colliding particles masses. Thus, the particles that can be produced are determined by the centre of mass energy of the colliding particles (denoted by $\sqrt{s}$), which is a Lorentz invariant magnitude.

In two particle systems of masses m_1 and m_2 the total centre of mass energy can be expressed in the Lorentz-invariant form

$$M \equiv E_{cm} = [(E_1 + E_2)^2 - (\mathbf{p_1} + \mathbf{p_2})^2]^{1/2}, \tag{1}$$

where $c = 1$ and M is now defined as the **invariant mass**. As it can be seen in section 3, the concept of invariant mass is essential in the analysis of the produced particles.

Another relation that will be useful in the analysis, is the centre of mass momentum dependence on the invariant mass on two particles systems [8]:

$$q \equiv p_1 = p_2 = \frac{[(M^2 - (m_1 + m_2)^2)(M^2 - (m_1 - m_2)^2)]^{1/2}}{2M}. \tag{2}$$

The analysis is performed as function of certain kinematic variables. Because of their properties under Lorentz transformations, two variables are commonly used in this type of analyses: the transverse momentum and the rapidity.

The **transverse momentum** (p_T) corresponds to the component of linear momentum which is transverse to the beam direction. For this reason, it is a Lorentz invariant.

The **rapidity** (y) is defined as

$$y = \frac{1}{2} ln \frac{E + p_z}{E - p_z}, \tag{3}$$

where E is the energy of the produced particle and p_z is the momentum component of the particle parallel to the trajectory of the interacting beams. A particle with $y = 0$ has a transverse trajectory to the collision axis, while in the limit $y \to \infty$ the particle is parallel to the beam direction, being the sign of y chosen by convention with respect to one of the incident particles. The asymmetry in the beam energies in our proton-lead collisions produces a Lorentz boost in rapidity of $y_{boost} \approx 0.465$ in the direction of the proton beam, so it has to be taken into account when computing the centre of mass rapidity (y^*).

Another variable is commonly used: the **pseudorapidity**. It is defined as

$$\eta = -\ln \left[\tan \left(\frac{\theta}{2} \right) \right], \tag{4}$$

where θ is the angle between the produced particle and the trajectory of the colliding beams. It can be proved that in the ultra-relativistic limit, where the particle mass can be neglected, $y \approx \eta$. Since $\cos\theta = p_z/p$, the variable η allows to perform a kinematic analysis without knowing the mass of the final-state particle. In this analysis the pseudorapidity is not used to measure the kinematic dependence, but to determine the detector acceptance for charged particles.

The produced inelastic interactions in high energy collisions are commonly theoretically described by the four-momentum squared (Q^2) exchanged between the interacting partons, which are the constituents of nucleons, and the so called Bjorken-x, which is the momentum fraction of the nucleon in the nucleus carried by the parton which has interacted. The value of x can be approximated from the kinematics of the produced particle with the following expression [9]:

$$x \approx \frac{m_T}{\sqrt{s}} e^{-y}, \tag{5}$$

where m_T is the so called transverse mass, defined as $m_T = \sqrt{m^2 + p_T^2}$, being m and p_T the mass and the transverse momentum of the produced particle. The squared transverse mass m_T^2 can be also used to approximate Q^2.

1.3.1 Saturation region and Cronin effect

QCD calculations predict that at low values of x the gluon density in the proton and the nucleus increases strongly. This behaviour was also experimentally seen [12]. The theory

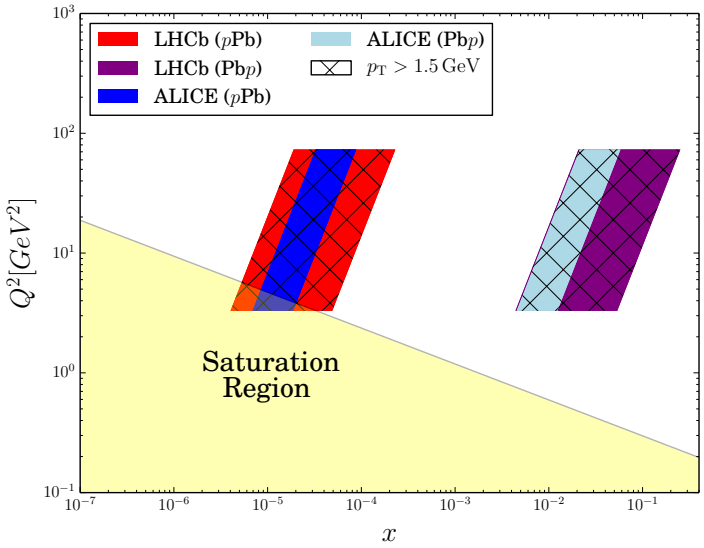

Figure 2: Kinematic coverage of LHCb and ALICE experiments corresponding to the ϕ meson detection for pPb and Pbp configurations. The Q^2 is approximated as the transverse mass of the produced particle: $Q^2 \approx m_T^2 = m^2 + p_T^2$, where m=1.02 GeV/c^2 corresponds to the ϕ meson mass. A dependence given by equation 5 is assumed. The parameterisation of the saturation region limit shown in the figure is given by $Q^2_{s,\mathrm{Pb}} = 0.26A^{1/3}(x_0/x)^{\lambda}$, where $\lambda = 0.288$, $x_0 = 3 \cdot 10^{-4}$ and A=208 [10, 11].

requires the existence of an upper limit for the occupation number of gluons. When this regime (named saturation region) is reached, the QCD dynamics can be described by the so called Colour Glass Condensate (CGC) effective field theory [13]. The CGC theory can be applied in proton-nucleus collisions in order to predict particle production cross sections for kinematics dominated by the low x contribution. In general, the models based on this approach predict a suppression of charged particle production in $p-A$ collisions relative to $p-p$ collisions.

Since 1975, different measurements have revealed an enhancement of the hadron production around 2 GeV/c < p_T < 3 GeV/c in proton-nucleus collisions with respect to scaled $p-p$ collisions [14]. Such effect is called Cronin effect, and its theoretical explanations are usually made in terms of multiple parton interactions in the large x regime. There are some studies that seem to reveal that the Cronin effect is larger in high multiplicity collisions [15]. This dependence of the Cronin effect on the multiplicity could be observed in this analysis.

Thus, the presence of saturation region effect is expected for low x processes while the Cronin effect arises in the large x regime. As it can be seen in Figure 2, the kinematic coverage of the LHCb detector is different for the two possible configurations of the collision. For the pPb configuration much lower values of x are covered in comparison with the ones covered in the Pbp configuration. Therefore, the saturation region effect should be predominant in pPb collisions while the Cronin effect should appear in the Pbp configuration.

1.4 Observables

The observables have been selected in such a way that the effect of the detector efficiency is minimised. Two ratios are constructed in order to cancel unwanted efficiency factors:

Ratio Central Peripheral (RCP) Corresponds to the ratio between the yield of high multiplicity processes (or central processes, by analogy with fully overlapping heavy-ion collisions) and low multiplicity processes (or peripheral). Thus, some efficiency factors such as the corresponding to the acceptance of the detector are cancelled. The efficiency factors that have some dependence on the multiplicity, such as the efficiency of the track reconstruction (see section 2.1.1), are still present. Mathematically, the magnitudes defined on (6) and (7) are measured in the analysis.

$$\mathrm{RCP}(p_T)_{High/Low} = \frac{(dN/dp_T)_{High}}{(dN/dp_T)_{Low}} \quad ; \quad \mathrm{RCP}(p_T)_{High/Medium} = \frac{(dN/dp_T)_{High}}{(dN/dp_T)_{Medium}}; \quad (6)$$

$$\mathrm{RCP}(y^*)_{High/Low} = \frac{(dN/dy^*)_{High}}{(dN/dy^*)_{Low}} \quad ; \quad \mathrm{RCP}(y^*)_{High/Medium} = \frac{(dN/dy^*)_{High}}{(dN/dy^*)_{Medium}}. \quad (7)$$

where N is the ϕ meson yield and the sub-index $High$, $Medium$ and Low refers to the different multiplicity classes.

Double ratio ($\mathscr{R}$) Defined as the ratio between the RCP corresponding to the pPb configuration and the one corresponding to the Pbp configuration. If the multiplicity classes are properly defined for both configurations, this ratio cancels the multiplicity dependence of the detector efficiency, leading to a more unbiased observable. Mathematically:

$$\mathscr{R}(p_T)_{High/Low} = \left.\frac{\mathrm{RCP}(p_T)_{p\mathrm{A}}}{\mathrm{RCP}(p_T)_{\mathrm{A}p}}\right|_{\frac{High}{Low}} \quad ; \quad \mathscr{R}(p_T)_{High/Medium} = \left.\frac{\mathrm{RCP}(p_T)_{p\mathrm{A}}}{\mathrm{RCP}(p_T)_{\mathrm{A}p}}\right|_{\frac{High}{Medium}}; \quad (8)$$

$$\mathscr{R}(y^*)_{High/Low} = \left.\frac{\mathrm{RCP}(y^*)_{p\mathrm{A}}}{\mathrm{RCP}(y^*)_{\mathrm{A}p}}\right|_{\frac{High}{Low}} \quad ; \quad \mathscr{R}(y^*)_{High/Medium} = \left.\frac{\mathrm{RCP}(y^*)_{p\mathrm{A}}}{\mathrm{RCP}(y^*)_{\mathrm{A}p}}\right|_{\frac{High}{Medium}}. \quad (9)$$

In these double ratios it is not possible to individually observe the presence of the expected effects in each configuration, but their combined effect is manifested. The results will be interpreted in terms of the above mentioned effects and the underlying theory for different multiplicity classes. It can be also verified whether the obtained results are consistent with other experimental observations.

2 Experimental approach

2.1 The LHCb detector

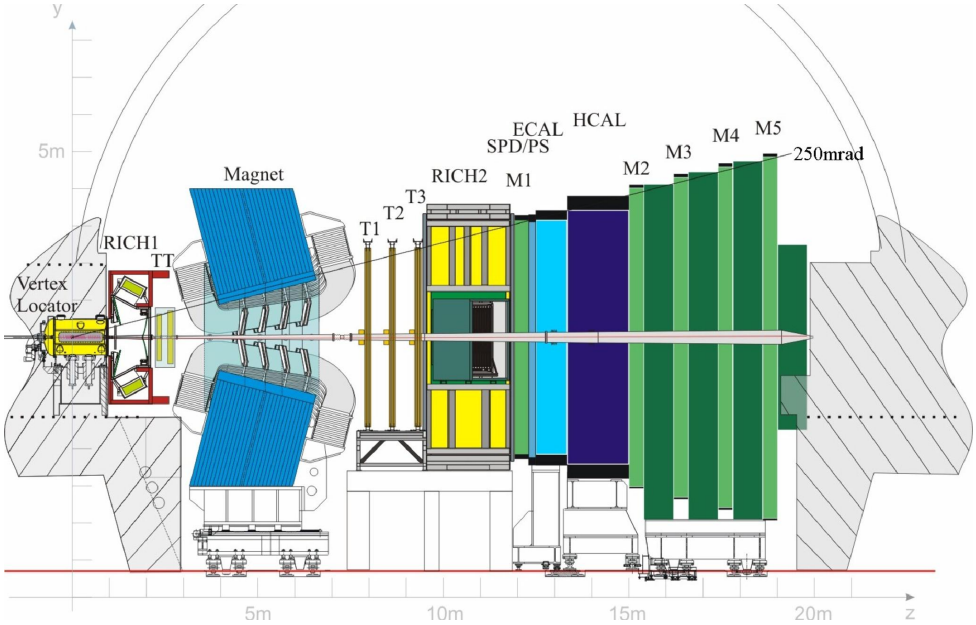

Figure 3: View of the LHCb detector [16]. In the figure the Vertex Locator (VELO), the Tracking System (composed by the TT and T1-T3 stations), the Ring Imagin Cherenkov (RICH) detectors, the calorimeters (ECAL and HCAL), the muon system (composed by stations M1-M5) and the magnet (required for the momentum measurement of the charged particles) are shown. The collisions take place inside the VELO in the y-axis of the figure.

The LHC*b* detector is a single-arm forward spectrometer originally designed for precision measurements of CP violation and rare decays of beauty and charm hadrons. The detector is placed in the Large Hadron Collider, a particle accelerator formed by a 27 km ring at CERN.

The detector has an angular acceptance which goes from 10 mrad to 300 mrad on the bending plane and from 10 mrad to 250 mrad on the non bending plane. In Figure 3 the different detector elements can be seen. The ones which are particularly relevant to this analysis are the Vertex Locator (VELO) that allows the determination of the position of the collision point, known as primary vertex (PV), the tracking system that provides a measurement of the momentum (p) of charged particles and the two ring-imaging Cherenkov detectors that are used to discriminate between different species of charged particles (in particular, protons, pions and kaons).

The detector must cope with the large number of hadrons produced in the collisions. This requires an efficient, robust and flexible trigger that assumes the harsh hadronic environment. The trigger must be sensitive to many different final states. Excellent vertex and momentum resolution are essential for a good proper-time resolution, necessary for a good invariant mass resolution, needed to reduce the combinatorial background [17]. Now, a brief overview of the experimental setup is presented.

2.1.1 Track reconstruction

The track reconstruction software combines the hits of the following sub-detectors to form charged particle trajectories from the VELO to the calorimeters. The reconstruction algorithm aims at finding all tracks in the event which leave enough detector hits.

Vertex Locator (VELO) The Vertex Locator (VELO) is a silicon microstrip detector that surrounds the $p-$Pb interaction region. It is formed by 21 stations, placed along and perpendicular to the beam axis where there is negligible magnetic field. The VELO provides measurements of track coordinates which are used to identify the PV and the secondary vertices. The VELO was designed to optimise the LHCb physics program in the following ways:

- **Angular coverage**. It covers just 1.8% of the solid angle but, as an example, the detector fully reconstructs roughly 27% of $b\bar{b}$ production for 7 TeV proton-proton centre of mass collisions. The VELO reconstructs tracks in the forward direction and also backward direction which does not have momentum information, but are useful to improve the primary vertex reconstruction. Thus, the VELO is the sub-detector with the largest angular coverage. For this reason, the VELO measurements are used in section 3 to characterise the multiplicity of each collision.
- **Triggering**. The reconstruction of the primary vertex and the displaced secondary decay vertex of a heavy flavour hadron in the VELO is a key ingredient of the high level trigger which reduces the event rate.
- **Efficient reconstruction**. High efficient cluster reconstruction in the VELO allows LHC*b* to study decay modes with up to six charged tracks in the final state.
- **Displaced tracks and vertices**. Excellent vertex resolution is essential to the LHC*b* physics programme.
- **Decay time**. The decay time of a particle can be obtained from the measurement of its flight distance in the VELO.

The VELO system is operated in vacuum and uses a bi-phase CO_2 cooling system. In order to maximise the PV location precision, the sensors are moved to 7 mm from the LHC beam for physics data taking. This distance is smaller than the aperture required by the LHC beam during injection, so the detector is produced in two retractable halves.

Tracking system In addition to track reconstruction, the tracking system performs a precise measurement of the momentum. It consists of four planar tracking stations: the Tracker Turicensis (TT), which is placed upstream of the dipole magnet covering the full acceptance, and the T1-T3 stations placed downstream the magnet. As well as the VELO, the TT and the inner part of the T1-T3 stations (Inner Tracker, IT) are based on silicon microstrips. The TT and the IT were developed in a common project called the Silicon Tracker (ST).

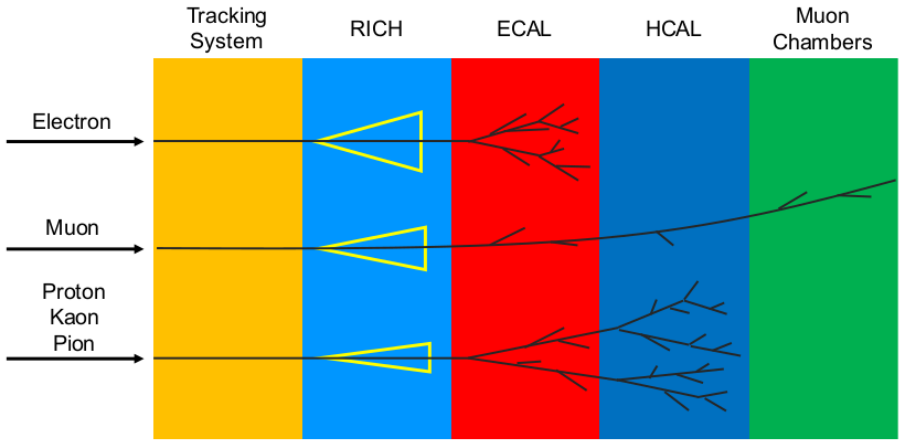

Figure 4: Ilustration of the responses of different particles in the LHC*b* detector [18].

In the outer region of T1-T3 stations (Outer Tracker) straw-tubes are employed. Basically, these straw-tubes are gas filled tubes with a wire along their axis. A high voltage is applied between the wire and the tube so that an electric field is present in the gas filled area. When a charge particle transverses the straw tube, ionisation takes place. The Outer Tracker has a worse spatial resolution than the Silicon Tracker, but it was much cheaper and is suitable for this region because the particle flux is smaller.

2.1.2 Particle identification (PID)

Combining the information of the Ring Imaging Cherenkov detectors, the hadronic and electromagnetic calorimeters, and the muon chambers, the particle identification (PID) algorithm (based on machine learning) classifies the reconstructed tracks as concrete charged particles. More information about the identification process is presented in section 3.

Ring Imaging Cherenkov (RICH) detectors Formed by two stations: RICH1, an upstream detector that covers the low momentum charged particle range, and RICH2, a downstream detector limited to the high momentum region. The Cherenkov radiation produced by the passage of a particle is measured by using a system of mirrors. The RICH detector allows the calculation of the particles velocity thanks to the dependence of it on the angle of the cone of light.

Calorimeters The calorimeters stop the impacting particles measuring their energy loss. The calorimeter system is composed by several layers: the Scintillating Pad Detector (SPD), the Preshower (PS), an electromagnetic calorimeter (ECAL) and a hadronic calorimeter (HCAL). It provides the identification of electrons, photons and hadrons and measures their energies and positions.

Muon system It is composed of five stations (M1-M5) of rectangular shape that provide muon identification.

2.1.3 Trigger

The LHC*b* trigger reduces the large amount of data generated in the collisions by pre-selecting events with interesting physics signatures for study. It is organised in two stages named Level-0 (L0) and High Level Trigger (HLT). The L0 uses information of the VELO, the calorimeters and the muon system to reduce the event rate from the nominal LHC bunch crossing rate of 40 MHz to a maximum of 1.1 MHz. The HLT is a software layer that performs an exhaustive selection based on the full event reconstruction, further reducing the rate of stored events.

2.2 The $\phi(1020)$ meson

Since the $\phi(1020)$ meson is the lightest bound state of strange quarks ($s\bar{s}$) it is copiously produced in hadronic collisions, so it is a good choice for this analysis. It has a rest mass of $M = 1919.461 \pm 0016$ MeV/c^2 and a width of Γ=4.249±0.013 MeV/c^2 [8]. It decays into a pair of kaons K^+K^- with a branching ratio of (49.2±0.5) %, being the most probable decay mode.

As it can be seen in section 3, the detection procedure of the ϕ meson relies on the identification of the produced kaons in the above mentioned decay. Each kaon is identified by the PID system and classified as K^+ (with positive charge) or K^- (with negative charge) depending on the trajectory of the reconstructed track and the magnet polarisation.

Detection efficiency There are some limitations to the particle detection. The limited accuracy of the track reconstruction or the fraction of particles that escape from the detector acceptance are just some of the various factors that reduce the detector efficiency. There is also a small fraction of the selected candidates for the analysis that may be wrongly selected (in particular, a miss-identification of a kaon) (see section 3.2). In addition, some efficiency factors like the corresponding to the track reconstruction have an evident dependence on the multiplicity of the event.

These biases are not corrected in the analysis, and this must be taken into account when interpreting the results. In order to obtain non biased results the efficiency effects are minimised by performing ratios between quantities affected by the same efficiency factors, such as the RCP and the double ratio $\mathscr{R}$ which were already explained in section 1.4.

3 Analysis

In this section the definition of the different multiplicity classes and the signal extraction is performed. The invariant mass method is used: since the decay channel $\phi \to K^+K^-$ is the most probable, the detection method consists of the measurement of the resonance created by the correlated kaons on the invariant mass spectrum. Such resonance, is described by a Breit-Wigner function centred on the ϕ meson mass protruding above the background generated by uncorrelated kaons.

3.1 Proton-lead data

The data set of the proton-lead collisions used in this analysis was taken in February 2013. The proton beam energy was E_p=4 TeV, while the energy per nucleon of the lead beam was E_{Pb}=1.58 TeV/nucleon, leading to a nucleon-nucleon centre of mass energy of $\sqrt{s_{NN}} = 5.02$ TeV. The average instantaneous luminosity during the data taking was $\mathcal{L} = 3 \cdot 10^{27}$ cm^{-2}s^{-1} and the total integrated luminosity was $\mathcal{L} \approx 1.5$ nb^{-1}.

There are four available data samples: for each configuration (pPb or pA, forward and Pbp or Ap, backward), measurements for two different polarities of the magnet were taken. As it would be expected from the symmetry of the system, the polarity of the magnet does not impact the result of the analysis. After verifying this assumption, the analysis is performed using the contribution of both of the magnet polarities together.

The information is stored on n-tuples in such a way that the different variables are accessible for each event. These tuples are analysed using the ROOT [19] `TTree` class.

3.1.1 Simulated samples

For each data set, a simulated sample generated by EPOS [20] is available. The simulated samples consist on two sub-samples: one contains the real information of a simulated collision, while the other contains the reconstruction and particle identification obtained with the LHC*b* software. In these simulation samples the number of proton-lead interactions is fixed to one. These samples are commonly used to quantify biases induced by the detector. As it can be seen in the following sections, simulated samples play an essential role in this analysis when defining different multiplicity classes.

3.2 Selection cuts

In order to successfully perform the analysis, a suppression of the background coming from random combinations of tracks is needed. The PID algorithm provides a classifier named `ProbNN`, which is based on six binary one-layer artificial neural networks. Each of these networks corresponds to one particle type and is trained to separate this particle type from all others [18]. This classifier is used to select the particles with a significant probability of being kaons. In this way, most of the particle pairs will be two kaons and those that come from the same ϕ meson desintegration will contribute to the Breit-Wignet signal. The chosen requirements are `Kpl_ProbNN>0.3` (for the K^+) and `Kmi_ProbNN>0.3`

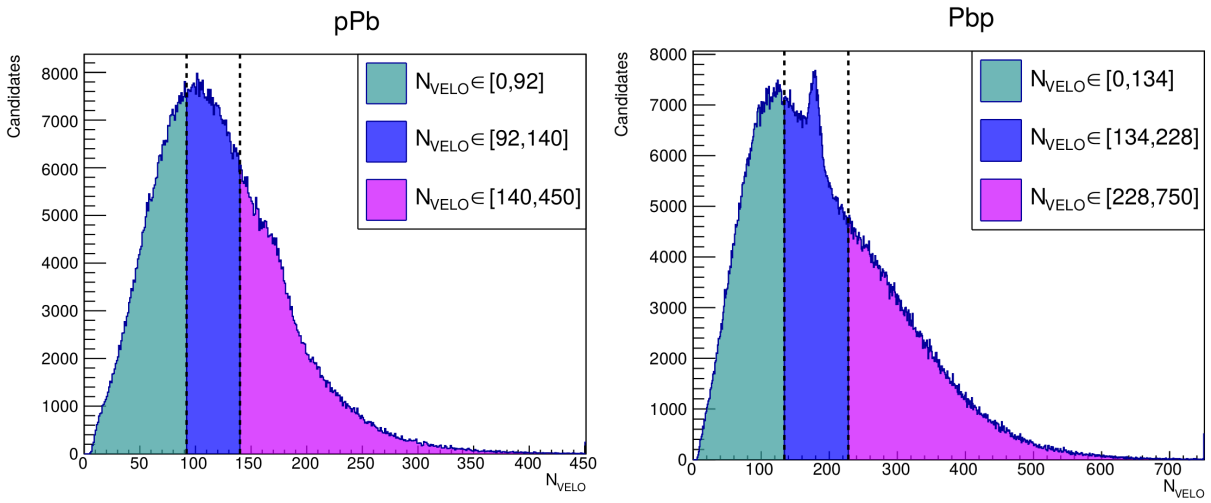

Figure 5: The number of detected candidates is shown as function of the number of VELO tracks measured in the event for pPb (left) and Pbp (right) configurations. The spectra are divided in three parts with the same number of cantidates.

(for the K^-). In addition, the condition of the existence of a single primary vertex (PV) is imposed through the variable `nPVs=1`.

The kinematic binning is also performed imposing the corresponding cuts: the ϕ transverse momentum (`phi_PT` variable) is limited between 1 and 7 GeV/c, while the rapidity is constraint to the $2.5<y^*<4.3$ range. In the case of the rapidity, it has to be calculated as function of other given variables through (3) and the corresponding Lorentz boost has to be taken into account.

In the case of the simulation samples, the evaluated acceptance of the detector is constrained using the pseudorapidity (η) in the laboratory frame. In order to remove the signals coming from elastic interaction, η is limited between $2<|\eta|<5$.

3.3 Determination of multiplicity classes

The variable `nVeloTracks`, which corresponds to the number of tracks reconstructed on the VELO in each event, is used as an indicator of the number of charged particles. In order to decide how to define different multiplicity classes, the `nVeloTracks` (N_{VELO}) spectra are studied. A first classification based on the division of the N_{VELO} spectrum in three quantiles is made (named terciles). The results of such division can be seen in Figure 5. The peak that can be seen in the region of $N_{VELO} \approx 200$ (particularly prominent in Pbp configuration) is believed to come from secondary desintegrations in the VELO region. In any case, such phenomenon in the N_{VELO} spectrum does not influence this analysis.

As it can be seen, the collisions in the backward configuration lead on average to higher N_{VELO} values. A relation between the number of charged particles and N_{VELO} is needed in order to define common multiplicity classes.

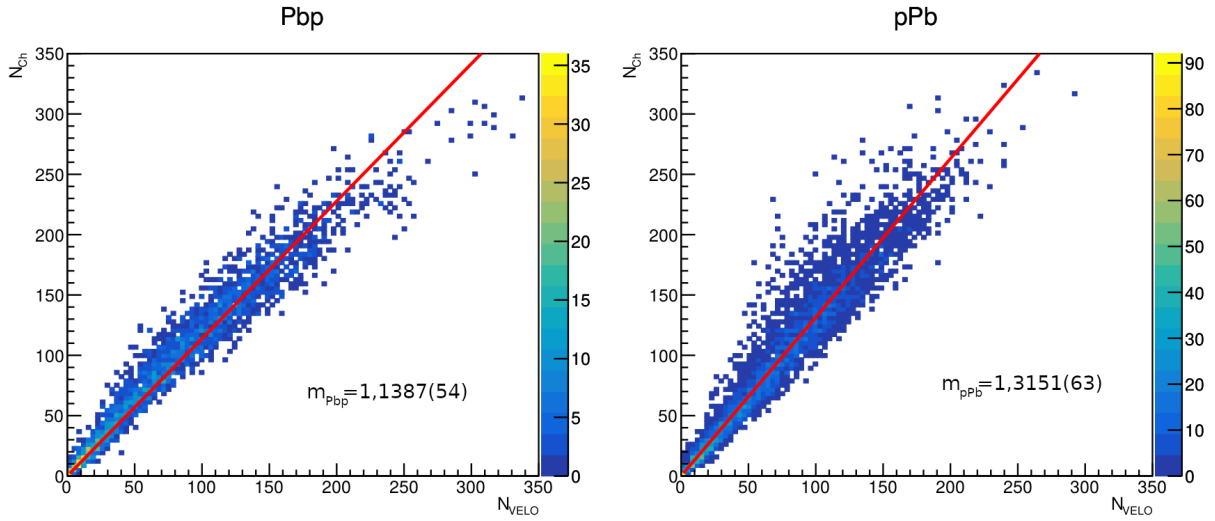

Figure 6: N_{Ch} vs N_{VELO} plots generated using the simulated samples for Pbp (left) and pPb (right) configurations. Since it seems to be reasonable to assume a linear dependence, a fit to the $N_{Ch} = m \cdot N_{VELO}$ function is made. The corresponding result for each configuration is also shown in the plot.

	Number of charged particles	
	Pbp configuration	**pPb configuration**
First N_{VELO} tercile	0 - 152.58(72)	0 - 120.99(58)
Second N_{VELO} tercile	152.58(72) - 259.6(12)	120.99(58) - 184.11(88)
Third N_{VELO} tercile	259.6(12) - ∞	184.11(88) - ∞

Table 1: Boundaries of the terciles defined in Figure 5 expressed in number of charged particles.

VELO tracks - charged particles relation

The relation between the VELO tracks and the number of charged particles (N_{Ch}) is calculated using the simulated samples, where the variable corresponding to N_{Ch} is available.

For both forward and backward configurations a N_{Ch} vs N_{VELO} plot is shown in Figure 6. Assuming a linear relation, a fit to the data is made. Since the independent coefficient is fixed to 0, the slope m of the fits gives, for each configuration, the relation between both variables.

Using those coefficients, the corresponding number of charged particles for the first VELO tracks spectra division made in Figure 5 is calculated. The results are shown in Table 1.

Now, this N_{VELO}–N_{Ch} relation is used to define common multiplicity classes so that the number of charged particles range is the same for each multiplicity class in both configurations. An arbitrary number of charged particles can be selected as limit between each multiplicity class. The m factor relates this number with the corresponding N_{VELO} value, so that the selection cuts can be imposed through the `nVeloTracks` variable.

	$\mathbf{N_{Ch}}$	$\mathbf{N_{VELO}(Pbp)}$	$\mathbf{N_{VELO}(pPb)}$
Low - Medium multiplicity boundary	137	120	104
Medium - High multiplicity boundary	222	195	169

Table 2: Definition of the number of charged particles that form each multiplicity class boundary. The corresponding N_{VELO} value for each boundary and configuration is shown.

For each boundary selection, a mean value between the corresponding terciles shown in Table 1 for each configuration is taken. In Table 2 the defined limits as well as the corresponding N_{VELO} value for each configuration are shown.

3.4 Signal yield extraction

Once the multiplicity classes are defined, the signal yield extraction is made for each one of them. The selection cuts explained in section 3.2 and the appropriate `nVeloTracks` restriction for each multiplicity class are imposed.

The results of the analysis are reported in terms of the transverse momentum p_T and of centre of mass rapidity y^* of the $\phi(1020)$ meson. First, a p_T binning is chosen for $y^* \in [2.5, 4]$. The employed bin limits are: $p_T = [1.0, 1.5, 2.0, 2.5, 3.0, 3.5, 4.0, 4.5, 5.0, 6.0, 7.0]$ GeV/c. Then, the p_T is integrated in $[1.0, 7.0]$ GeV/c and a y^* binning is proposed. The y^* bin limits employed are $y^* = [2.5, 3.0, 3.5, 4.0, 4.3]$.

It is important to take into account that the rapidity values stored in the n-tuples are given in the laboratory frame. Since the p and the Pb beams have different energies, the centre of mass of the system moves in the direction of the incident particle, so a different Lorentz boost must be taken into account to convert y into its centre of mass value y^* depending on the configuration. The Lorentz boost is $y^* = y - 0,465$ for the pPb configuration and $y^* = y + 0,465$ for Pbp one. As it has already been mentioned, the rapidity restriction is chosen in order to suppress the elastic interactions, and also in such a way the forward and backward y ranges overlap after considering the Lorentz boost.

3.4.1 Data set fit

The $\phi(1020)$ signal is modeled using a Voigtian function, which is a convolution of the Breit-Wigner corresponding to the resonance and a Gaussian function. The Gaussian contribution is needed because the limited resolution of the detector makes the signal of the invariant mass spectrum wider than the ϕ meson width. The Gaussian width σ, which is left as a free parameter of the fit, accounts for such effect, while the width of the Breit-Wigner is fixed to the tabulated ϕ meson width $\gamma = 4.249$ MeV [8].

The background is parameterised using the function (10).

$$f(M) = q \cdot m_b^{a_1} \cdot e^{-a_2 \cdot m_b}, \tag{10}$$

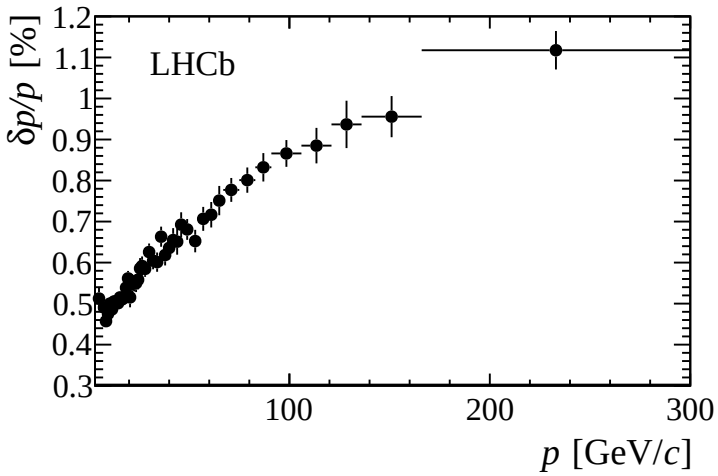

Figure 7: Relative momentum resolution versus momentum for long tracks in data obtained using J/ψ decays [16].

where q is the momentum defined on (2), which accounts for the K^+K^- phase space. Then, m_b is defined as $m_b = M(K^+K^-) - 2m_K$ being m_K the tabulated kaon mass and a_1 and a_2 are free parameters in the fit. This function was selected to model the background after considering a polynomial function, which did not reproduce well the background. The signal and background distributions are normalised by n_ϕ and n_{Bkg} respectively, which are free parameters. The n_ϕ variable corresponds to the yield of ϕ mesons.

The fits are performed using the `RooFit` tool [21], which allows to fit various histograms simultaneously. Since the signal shape must be the same for each multiplicity class, the fit of the signal for different classes can be performed simultaneously. The reason why the signals corresponding to different p_T bins are not fitted simultaneously is that the detector resolution has a dependence on p_T (see Figure 7), so the σ width has to be calculated separately for each p_T bin.

Due to the large number of fitted spectra, only two examples are shown on Figures 8 and 9. From each of them, the variable n_ϕ (from now on, named N) is extracted. The results are shown in Figures 10 and 11.

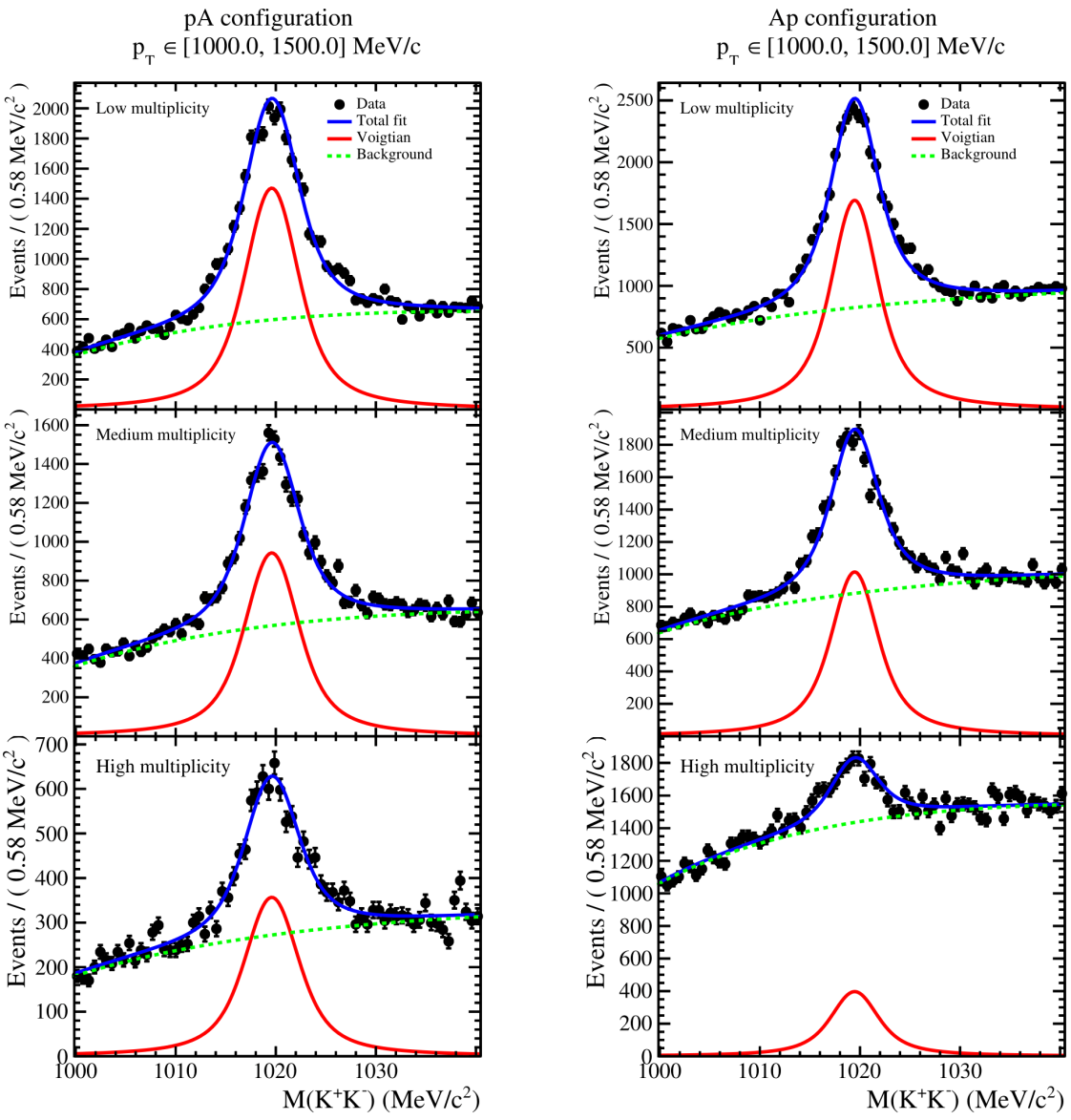

Figure 8: Fits of the invariant mass spectrum to a Voigtian plus a background function (equation 10) for the different multiplicity classes in the 1 GeV/c $< p_T <$ 1.5 GeV/c and the 2.5 $< y^* <$ 4 ranges. The left plots correspond to the Pbp configuration and the right ones to the Pbp configuration. The centre of the Voigtian function as well as the width of the Gaussian function, σ, are obtained simultaneously for the three multiplicity classes using the RooFit module.

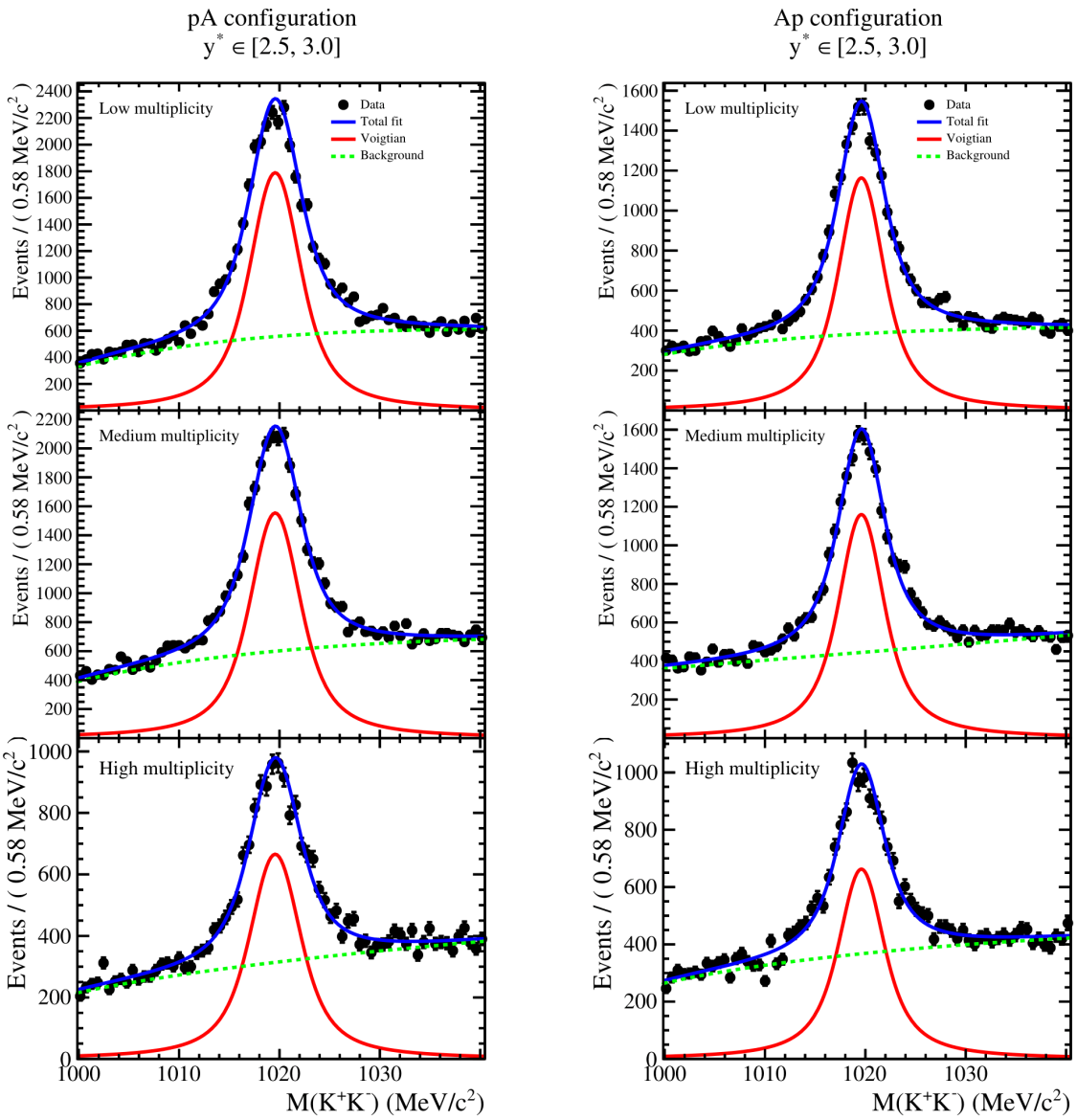

Figure 9: Fits of the invariant mass spectrum to a Voigtian plus a background function (equation 10) for the different multiplicity classes in the 1 GeV/c $< p_T <$ 7 GeV/c and the 2.5 $< y^* <$ 3 ranges. The left plots correspond to the Pbp configuration and the right ones to the Pbp configuration. The centre of the Voigtian function as well as the width of the Gaussian function σ are obtained simultaneously for the three multiplicity classes using the RooFit module.

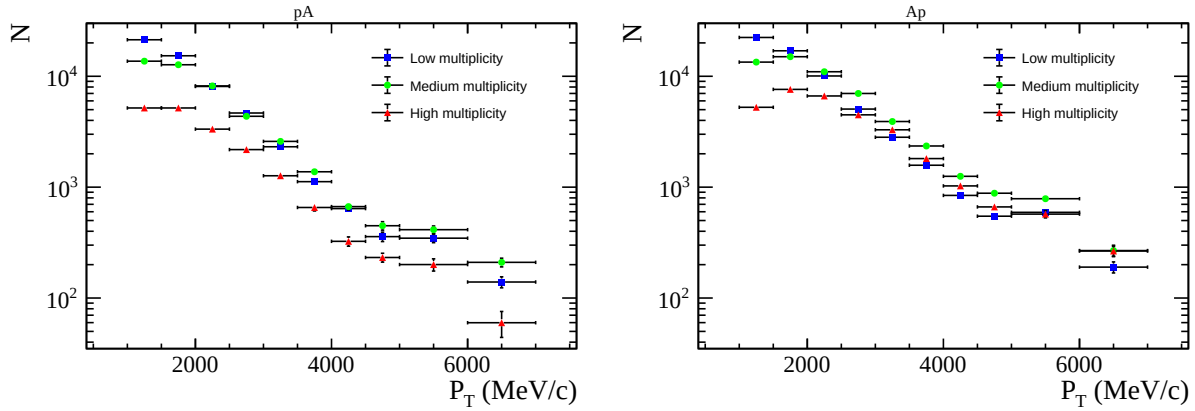

Figure 10: ϕ meson yields for different transverse momentum ranges and multiplicity classes for forward (left) and backward (right) configurations.

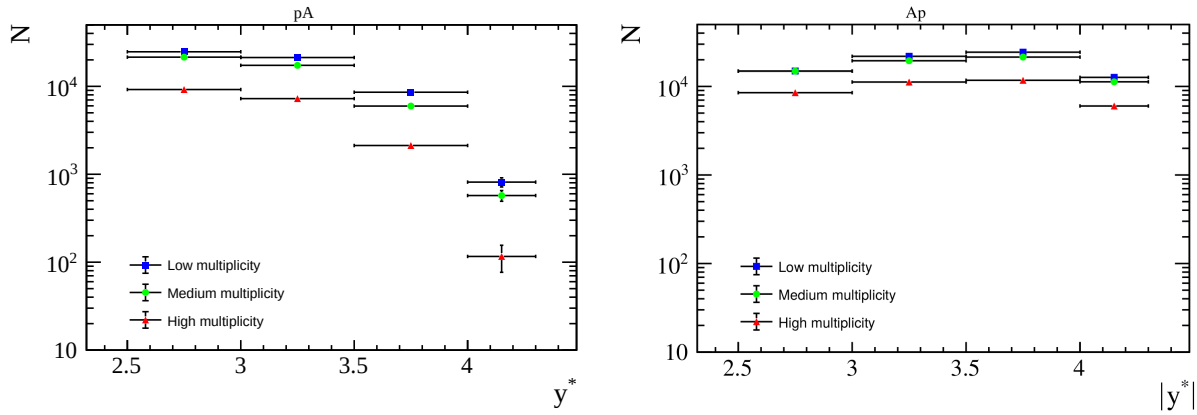

Figure 11: ϕ meson yields for different rapidity ranges and multiplicity classes for forward (left) and backward (right) configurations.

The ϕ meson yield for the different multiplicity classes for the pPb (pA) and Pbp (Ap) configurations can be seen for p_T and y^* bins in Figures 10 and 11, respectively. As already discussed, the efficiencies of the detector are not corrected in the figures. Non-trivial different efficiency factors may affect each yield value, so no further discussion is performed around these plots.

4 Results

The already introduced RCPs are calculated by performing the corresponding ratios of the yields shown in Figures 10 and 11. The uncertainties of such ratios are calculated propagating the corresponding yield uncertainties provided by the `RooFit` module. In a general form, RCP=$\frac{n_c}{n_p}$ and

$$u(\mathrm{RCP}) = \sqrt{\left(\frac{d\ \mathrm{RCP}}{dn_c}\right)^2 u^2(n_c) + \left(\frac{d\ \mathrm{RCP}}{dn_p}\right)^2 u^2(n_p)} \ = \ \sqrt{\frac{u^2(n_c)}{n_p^2} + \left(\frac{n_c}{n_p}\right)^2 u^2(n_p)}, \quad (11)$$

where the n variables are the extracted yields and the associated c and p sub-index refer to the central (high multiplicity) or peripheral (medium or low multiplicity) events.

The RCPs defined in equations (6) and (7) are respectively shown in Figures 11 and 12. The value of each RCP is calculated without normalising by the number of binary collisions. These factors may be taken into account in order to further isolate the multiplicity effects, but this is left for a future study. However, such factors are constant for each multiplicity class [15], so the slope of each RCP is not modified and some appreciations about them can be made.

In Figure 12 it can be seen that the slopes of the RCPs corresponding to the backward configuration are larger than the ones corresponding to the forward configuration. This tendency agrees with the expected presence of a Cronin effect in the backward configuration.

This observation is also consistent with other measurements made in different experiments. In [22] and [23] the so called nuclear modification factor is measured. The nuclear modification factor ($R_{p\mathrm{Pb}}$) is defined as the particle yield in $p-A$ collisions normalised by the corresponding yield in $p-p$ collisions and the number of binary nucleon-nucleon collisions. In such measurements an enhancement of $R_{p\mathrm{Pb}}$ in the backward configuration with respect to forward configuration is observed.

Concerning the multiplicity dependence, in the right plot of the Figure 12 (backward configuration) it can be seen that in the 3 GeV/c<p_T<4 GeV/c region the High/Low multiplicity ratio increases faster than the Medium/Low multiplicity ratio. The Cronin effect is expected in this p_T range and increases with the multiplicity [15], so it may contribute to this High/Low multiplicity ratio enhancement.

In the Figure 13 it can be seen a decrease of the RCPs when the rapidity increases. This decrease is larger in the forward configuration. It could be caused by the saturation effect.

Now a quotient between the RCPs corresponding to the different configurations is performed, leading to the $\mathscr{R}$ double ratios defined in equations (8) and (9). The corresponding uncertainties are calculated by propagating the corresponding RCPs uncertainties. In general:

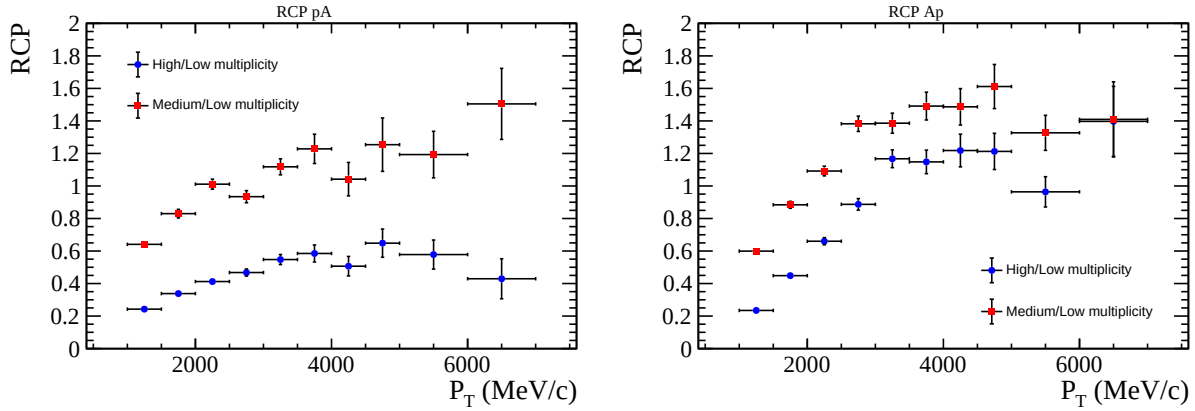

Figure 12: Ratio Central - Peripheral for different transverse momentum ranges and multiplicity classes for forward (left) and backward (right) configurations.

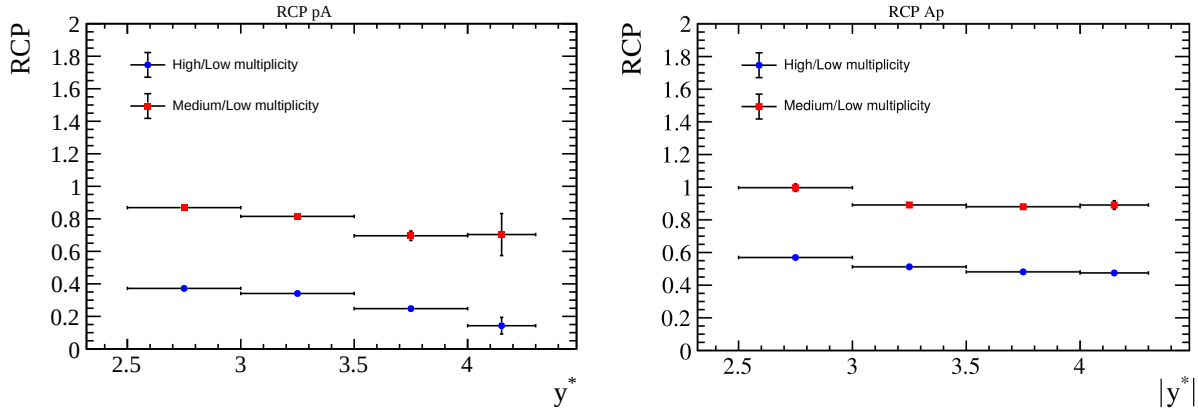

Figure 13: Ratio Central - Peripheral for different rapidity ranges and multiplicity classes for forward (left) and backward (right) configurations.

$$u(\mathscr{R}) = \sqrt{\frac{u^2(\mathrm{RCP}_{p\mathrm{A}})}{\mathrm{RCP}^2_{\mathrm{A}p}} + \left(\frac{\mathrm{RCP}_{p\mathrm{A}}}{\mathrm{RCP}^2_{\mathrm{A}p}}\right)^2 u^2(\mathrm{RCP}_{\mathrm{A}p})}. \tag{12}$$

The obtained double ratios ($\mathscr{R}$) are shown in Figure 14. Due to the previously explained considerations about efficiency cancellations, it can be assumed that, in first approximation, there is no constant factors biasing the measurement. The number of binary collisions does not depend on the configuration, so this factor that is not taken into account on the RCP plots should vanish by performing the forward/backward ratio.

In the left plot of Figure 14 it can be seen that the High/Low multiplicity $\mathscr{R}$ decreases faster than the Medium/Low multiplicity $\mathscr{R}$, taking smaller values in all the p_T range. This observation may be explained by the multiplicity dependence of the Cronin effect: the Cronin effect produces a larger enhancement of the yields in the backward configuration for high multiplicity events, but it does not take place in the forward configuration. Thus, due to its definition, $\mathscr{R}$ takes lower values for High/Low multiplicity ratios in comparison with Medium/Low multiplicity ratios.

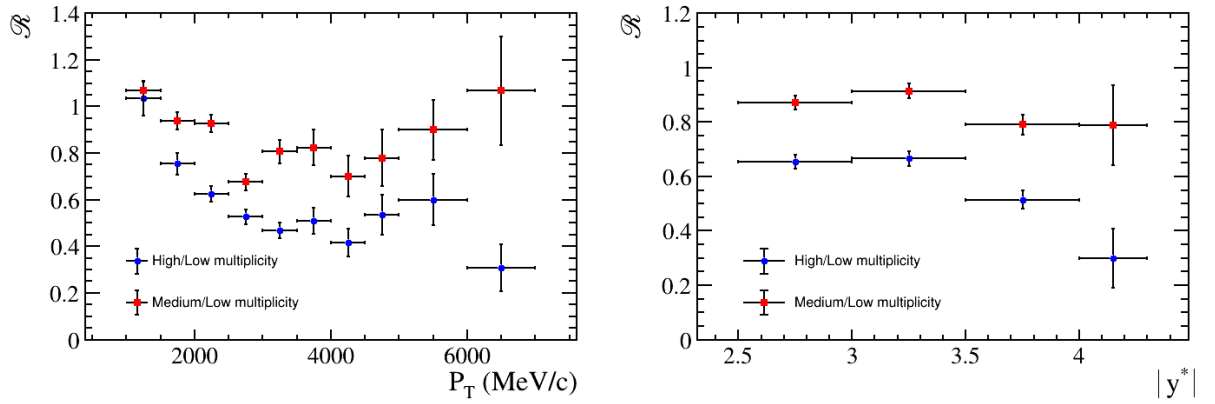

Figure 14: Double ratios for different transverse momentum ranges (left) and rapidity ranges (right).

In the right plot of the Figure 14 it can be observed that the value of $\mathscr{R}$ decreases as the absolute value of y^* increases. This could indicate that some collective initial effects like the already introduced saturation effect may be appearing. Such effects may decrease the forward configuration yields on the high rapidity region (low x region) leading to lower values of $\mathscr{R}$. The High/Low multiplicity $\mathscr{R}$ seems to decrease faster. In view of these results, it might be interesting for future experiments to study in more detail the influence of multiplicity on these type of effects.

5 Conclusions

This work contains a preliminary measurement of the multiplicity dependence of the ϕ meson production at $\sqrt{s}$ =5.02 TeV in $p-$Pb collisions. This is the first time that this analysis is performed in the chosen kinematic range. An observation of some multiplicity effects and a proposal of the effects that may be involved in the processes is provided.

This analysis of the multiplicity dependence is interesting because it allows to study the strangeness enhancement that has been recently measured for high multiplicity events. The origin of such enhancement, as well as other observations, like the already mentioned flow correlations in the particle production for $p-p$ collisions, are not fully understood, so further analyses following this trend should take place in the future.

It has been shown that the observed multiplicity dependence on the chosen observables (RCP and $\mathscr{R}$) is consistent with other experiments and could be explained as a consequence of some known effects like the Cronin effect or the saturation effect. Further studies and some improvements on this one can be made in the future. A detailed calculation of the efficiency factors using the simulated samples would correct the yield plots of Figures 10 and 11 and it could help to extract further information from them. Moreover, other interesting observables like the cross section of ϕ meson production could be calculated by knowing such efficiency factors.

References

[1] J. Rafelski, "Strangeness and quark–gluon plasma," *Acta Physica Polonica B*, vol. 43, 12 2011.

[2] J. Rafelski and R. Hagedorn, "From Hadron Gas to Quark Matter. 2.," in *International Symposium on Statistical Mechanics of Quarks and Hadrons*, 10 1980.

[3] E. V. Shuryak, "Quantum Chromodynamics and the Theory of Superdense Matter," *Phys. Rept.*, vol. 61, pp. 71–158, 1980.

[4] E. Andersen *et al.*, "Strangeness enhancement at mid-rapidity in Pb−Pb collisions at 158-A-GeV/c," *Phys. Lett. B*, vol. 449, pp. 401–406, 1999.

[5] M. Meissner, *Measurements of particle production and particle correlations in proton-proton and proton-ion collisions with LHCb*. PhD thesis, Heidelberg U., 2015.

[6] V. Khachatryan *et al.*, "Measurement of long-range near-side two-particle angular correlations in pp collisions at $\sqrt{s}$ =13 TeV," *Phys. Rev. Lett.*, vol. 116, no. 17, p. 172302, 2016.

[7] J. Adam *et al.*, "Enhanced production of multi-strange hadrons in high-multiplicity proton-proton collisions," *Nature Phys.*, vol. 13, pp. 535–539, 2017.

[8] P. Zyla *et al.*, "Review of Particle Physics," *PTEP*, vol. 2020, no. 8, p. 083C01, 2020.

[9] N. Armesto, "Nuclear shadowing," *J. Phys. G*, vol. 32, pp. R367–R394, 2006.

[10] K. J. Golec-Biernat and M. Wusthoff, "Saturation effects in deep inelastic scattering at low Q^2 and its implications on diffraction," *Phys. Rev. D*, vol. 59, p. 014017, 1998.

[11] H. Kowalski, T. Lappi, and R. Venugopalan, "Nuclear enhancement of universal dynamics of high parton densities," *Phys. Rev. Lett.*, vol. 100, p. 022303, Jan 2008.

[12] F. D. Aaron, C. Alexa, K. Alimujiang, V. Andreev, B. Antunovic, A. Asmone, S. Backovic, A. Baghdasaryan, E. Barrelet, and et al., "A precision measurement of the inclusive ep scattering cross section at HERA," *The European Physical Journal C*, vol. 64, p. 561–587, Oct 2009.

[13] F. GELIS, "Color glass condensate and glasma," *International Journal of Modern Physics A*, vol. 28, p. 1330001, Jan 2013.

[14] D. Antreasyan, J. W. Cronin, H. J. Frisch, M. J. Shochet, L. Kluberg, P. A. Piroué, and R. L. Sumner, "Production of hadrons at large transverse momentum in 200-, 300-, and 400-gev $p-p$ and p-nucleus collisions," *Phys. Rev. D*, vol. 19, pp. 764–778, Feb 1979.

[15] J. Adam *et al.*, "Centrality dependence of particle production in p-Pb collisions at $\sqrt{s_{\rm NN}}$= 5.02 TeV," *Phys. Rev. C*, vol. 91, no. 6, p. 064905, 2015.

[16] R. Aaij *et al.*, "LHCb Detector Performance," *Int. J. Mod. Phys. A*, vol. 30, no. 07, p. 1530022, 2015.

[17] A. Alves *et al.*, "The LHCb Detector at the LHC," *JINST*, vol. 3, p. S08005, 2008.

[18] Derkach, Denis, Hushchyn, Mikhail, and Kazeev, Nikita, "Machine learning based global particle identification algorithms at the lhcb experiment," *EPJ Web Conf.*, vol. 214, p. 06011, 2019.

[19] R. Brun and F. Rademakers, "ROOT: An object oriented data analysis framework," *Nucl. Instrum. Meth. A*, vol. 389, pp. 81–86, 1997.

[20] T. Pierog, I. Karpenko, J. M. Katzy, E. Yatsenko, and K. Werner, "EPOS LHC: Test of collective hadronization with data measured at the CERN Large Hadron Collider," *Phys. Rev. C*, vol. 92, no. 3, p. 034906, 2015.

[21] W. Verkerke and D. P. Kirkby, "The RooFit toolkit for data modeling," *eConf*, vol. C0303241, p. MOLT007, 2003.

[22] **LHCb** collaboration, "Measurement of the nuclear modification factor and prompt charged particle production in pPb and pp collisions at $\sqrt{s_{\rm NN}} = 5\,\text{TeV}$," *arXiv preprint arXiv:2108.13115*, Aug. 2021.

[23] J. Adam *et al.*, "ϕ-Meson production at forward rapidity in p-Pb collisions at $\sqrt{s_{NN}}$=5.02 TeV and in pp collisions at $\sqrt{s}$=2.76 TeV," *Physics Letters B*, vol. 768, pp. 203–217, 2017.